Active Sensing for Measuring Contact of Thin Film Gecko-Inspired Adhesives

Tae Myung Huh[1], Cheng Liu[2], Jiro Hashizume[3], Tony G. Chen[1], Srinivasan A. Suresh[1], Fu-Kuo Chang[2], and Mark R. Cutkosky[1]

***Abstract*—Active sensing provides a way to assess whether a thin film of gecko-inspired adhesive has made good contact with a surface. This knowledge is useful for applications like gripping objects in space where a failed grasp could lead to loss of the object. Our active sensing approach uses Lamb waves in thin bilayers, excited and detected by piezoelectric strips. From the theory, we describe how attenuation increases with contact boundary condition changes. We validated the theory using FTIR imaging, showing that attenuation increases as the contact area grows. Pull tests on different textures of acrylic plate show that the slope change of the signal can predict the maximum adhesion limit with a 10N window and predict impending failure with a detection rate >80%. Lifting a cylindrical object shows that the sensor can signal different types of failures with a detection rate >85%, associated with unstable grasping.**

***Index Terms*—Perception for grasping and manipulation, force and tactile sensing, active sensing, guided Lamb wave, contact sensing.**

I. Introduction

GECKO-INSPIRED adhesives have been investigated for climbing, perching and grasping robots [1]–[6]. For grasping, the adhesive has the advantage of being activated by an applied shear load, not by friction from a normal force. This property enables a small gripper to gently grasp objects with large curvature [1], [2], [7].

Although the limits of shear-activated adhesive grippers have been studied [1], [8], the real-time monitoring of adhesion quality remains relatively unexplored, especially for adhesive films. However, due to surface imperfections and unexpected variations in loading, there is always the possibility of failure. Hence it is desirable to have a robust system for monitoring the state of contact and to provide a warning of impending failure, particularly in critical applications such as grasping objects in space [3].

In a gecko-inspired adhesive, adhesion arises from Van der Waals forces between the microstructured adhesive and a mating surface. The available normal and shear force are direct functions of the real area of contact. One way to estimate this area of contact is to use frustrated total internal reflection (FTIR) in which light is transmitted through a thin transparent sheet. Where the adhesive contacts the sheet, the change in the index of refraction allows light to escape, which a digital camera can record. FTIR has been used to measure the performance of gecko-inspired adhesives on tiles [8], [9] and the toes of live geckos [10]. It has also been incorporated into a large gripper for flat panels [11]. However, it is not practical for most grippers because it only works on transparent materials and requires the camera to view the sheet from the back side. In other work, a capacitive sensor was used to estimate the contact area of gecko-inspired adhesives on a rigid tile [9]. However, this method is not suitable for flexible film grippers with arbitrary loading.

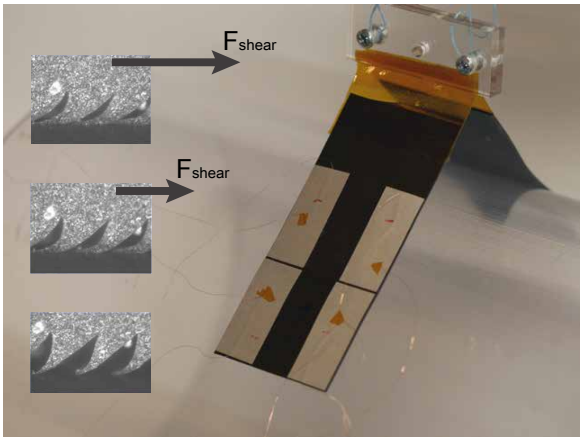

Fig. 1: (right) Flexible adhesive gripper with PVDF transducers. The left two transducers transmit guided Lamb waves and the right two receive them. (left) Microscope images show unloaded and loaded adhesive surfaces, demonstrating variation in contact area.

In this paper we present an approach for measuring the real area of contact that works for gecko-inspired adhesives on thin films. It involves active piezoelectric elements, as used in Structural Health Monitoring (SHM) [12], [13]. To evaluate soundness, active sensing uses the characteristics of a transmitted ultrasonic wave, such as attenuation, reflection, and scattering. This active sensing method was also explored to measure contact changes for an elastomer layer under compressive loads [14]. The approach analyzed the attenuation of Lamb waves induced by wave leakage, due to the stiffening of the elastomer layer. We expect similar Lamb wave attenuation in the gecko adhesive contacts due, in the

Manuscript received: February, 24, 2018; Revised May, 21, 2018; Accepted June, 14, 2018.

This paper was recommended for publication by Editor Ding, Han upon evaluation of the Associate Editor and Reviewers' comments. *Work supported by NSF NRI 1528145. Tae Myung Huh is supported by a Samsung Scholarship. Tony Chen is supported by the NSF GRF.

[1]T. M. Huh, T. G. Chen, S. A. Suresh and M. R. Cutkosky are with The Center for Design Research, Stanford University, Stanford, CA 94305, USA taemyung@stanford.edu

[2]C. Liu and F. Chang are with the Dept. of Aeronautics and Astronautics, Stanford University,Stanford, CA, USA

[3]J. Hashizume is with Hitachi America Ltd, Brisbane, CA, USA

Digital Object Identifier (DOI): see top of this page.

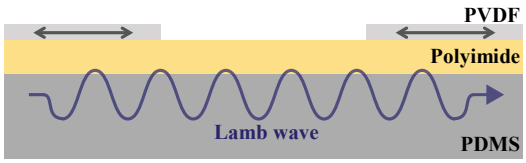

Fig. 2: Concept of active sensing on a flexible adhesive using Lamb waves. PVDF arrows show polarization direction.

present case, to increasing adhesive contact with a surface. In the following sections we first briefly review the theory behind Lamb wave propagation and attenuation in thin, bilayer films. We then present an active sensor that employs piezoelectric polymer films bonded to the back side of a film with a gecko-inspired adhesive (Fig. 1). We present experiments to characterize the sensor performance and show that the results agree with predictions from theory, with some variation due to manufacturing variability. We then present the results of an application-oriented experiment involving lifting a large cylinder using a gripper like that presented in [1]. We show that in over 80% of lifting cases we can predict impending contact failures before they would lead to dropping the object, even if only one side of the gripper is instrumented. We present conclusions and future work to increase the spatial resolution and accuracy of the sensing method for greater ability to predict possible failures.

II. Theory: Lamb wave in Gecko Inspired Adhesive

First, we consider Lamb wave propagation in a thin, layered structure. The adhesive consists of two layers: a polyimide film and a silicone rubber (PDMS) layer (Fig. 2). Approaches to compute the dispersion of Lamb waves in multiple layers include the global matrix method and transfer matrix method [15]. Because PDMS is viscoelastic, with high attenuation, the Lamb wave analysis on a viscoelastic bilayer is relevant [16]. We use the DISPERSE software [17] to analyze the Lamb wave in the material.

For the Lamb wave computation, we made two assumptions: a free boundary condition for the non-contact case and an ideal fixed boundary condition for a fully engaged contact. For the non-contact case, we assumed the boundary layer thickness corresponds to base of the wedges (Fig. 1, left) where the PDMS material becomes continuous. For the contact case, we assumed that the PDMS becomes a flat layer of increased thickness from the fully bent wedges. We model the contact surface as rigid because it is in general much stiffer than PDMS or polyimide film. The top of the polyimide film maintains free boundary conditions for both contact cases. The details of input parameters are given in Table I. We used the published attenuation property of a similar elastomer to PDMS [14].

The dispersion curves of M0 and M1 modes, for both contact cases are shown in Fig. 3. There was another lower phase velocity mode in this frequency range but it is omitted due to its high attenuation. The transition from free to fixed boundary conditions raises the frequency of the modes; surface adhesion increases the effective stiffness of the system, shifting the frequency to a higher range.

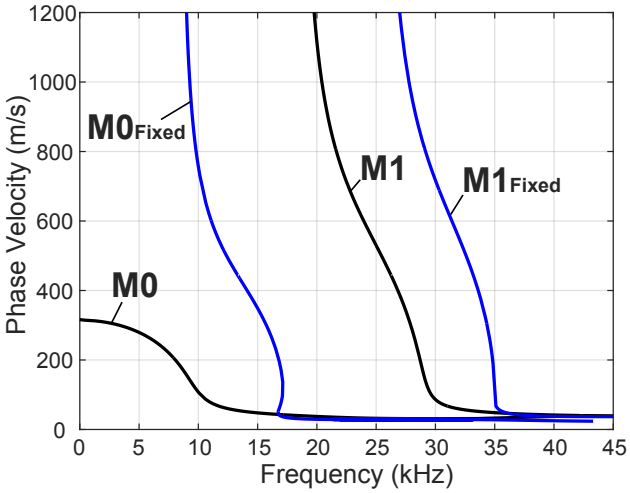

Fig. 3: Dispersion curves of the adhesive with parameters in Table I. M0, M1 are for the free boundary condition and $M0_{\text{Fixed}}$, $M1_{\text{Fixed}}$ are for fixed boundary (adhered).

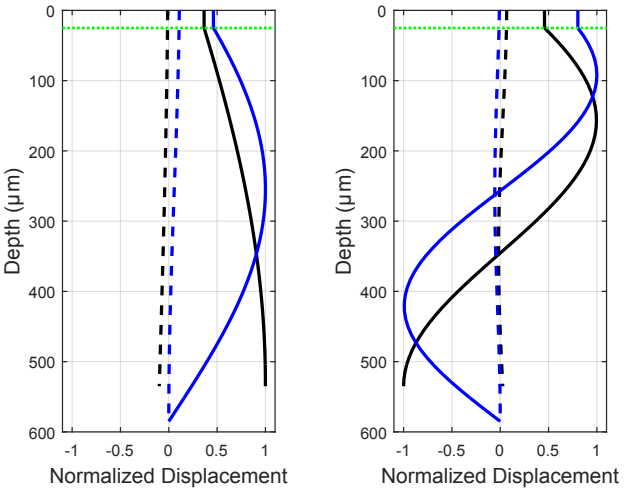

(a) M0 Mode (b) M1 Mode

Fig. 4: Mode shapes of M0 and M1. Values for depth $<25\,\mu$m (green dotted line) are for the polyimide film; beyond is for PDMS. Solid lines are in-plane displacements and dashed lines are out-of-plane displacements.

Between the two modes, we choose M1 for sensing because it is less affected by resonance of the substrate. In most Lamb wave analysis, resonance does not play a significant role because the substrate dimensions are assumed infinite. However, we are creating a guided Lamb wave in a small piece of adhesive film (39 x 85 mm), which can easily produce a resonance from reflection at the edges. This is not desired because a resonance around the frequency of interest makes it difficult to measure the attenuation. In addition, the frequency shift from the contact changes the resonance frequency, causing a potential overlap with the frequency of interest. The M1 mode has less chance to produce resonance because of its mode shape (Fig. 4). The dominant displacement variation occurs in the PDMS layer. A comparison with published single-layer mode shapes provides insight: the M0 is similar to a S0 mode, while M1 is similar to the A1 mode [15]. Studies on Lamb wave reflections at free ends show that in the lower

TABLE I: Material properties for dispersion curve. (*Value is for a similar elastomer at 300kHz [14]. **Polyimide assumed to have no attenuation.)

Material	Thickness (μm)	Density (g/cm^3)	Young's Modulus (Pa)	Poisson's Ratio	Longitudinal Attenuation (dB/cm)	Shear Attenuation (dB/cm)
Polyimide	25	1.42	2.5 G	0.34	0**	0**
PDMS (Sylgard 170)	510 -free 560 - fixed	1.35	1.59 M	0.499	3.5*	15*

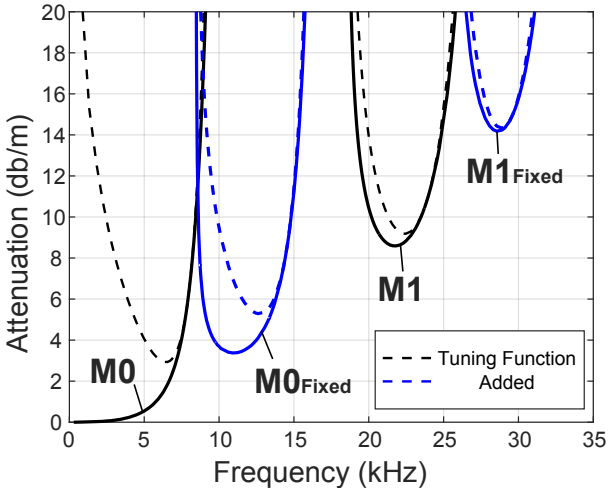

Fig. 5: Attenuation curve for free and fixed boundary conditions. Solid lines are attenuations from the gecko adhesive substrate. Dashed lines are attenuations from the substrate and the frequency tuning effect of a piezoelectric transducer. The plot is for a transducer of width $W = 13$ mm.

frequency ranges a reflection of the S0 mode remains S0 mode while the A1 reflection is mostly A0 mode [18]. Because the reflecting A1 mode changes its shape, it does not form a resonance across the substrate. Thus, the A1 mode is expected to have a frequency response without sharp resonance, which is beneficial for measuring attenuation.

Moreover, the attenuation curve shows greater difference from M1 to M1_{Fixed} than M0 to M0_{Fixed} (Fig. 5). To estimate the attenuation of the Lamb wave actuated by piezoelectric transducers, we added the frequency tuning effect to the attenuation of the substrate. Frequency tuning adjusts the frequency of maximum strain outputs by changing the width of a piezoelectric transducer. The relative strain amplitude can be estimated by the tuning function [13]:

$$g_{tune} = \sin(\pi f W / c_p) \tag{1}$$

where f is the wave frequency, c_p is corresponding phase velocity, and W is the width of the piezoelectric transducer along the wave propagation. The overall attenuation from the substrate and piezoelectric transducers can be obtained by subtracting the decibel value of eq. 1 from the substrate attenuation. For example, if W is 13 mm, the resultant attenuation curves are as dashed lines in Fig. 5. The minimum attenuation level in M0 mode to M0_{Fixed} increases by 2.4 dB and by 5.1 dB in M1 modes. The greater attenuation increase in the M1 mode allows better sensitivity.

The intermediate transition from a free boundary to a fixed boundary condition is difficult to simulate. However, it is expected that the similarity of the M1 and M1_{Fixed} modes allows more monotonic transitions than the M0 mode. The attenuation analysis predicts the minimum attenuation as the maximum strain frequencies shift by 5-10 kHz. Thus, the Lamb wave actuation signal should span at least 10kHz in the frequency domain to measure the attenuation.

III. Active Sensor Design for an Adhesive Film

A. Flexible Gecko-Inspired Adhesive Gripper

Gecko-inspired adhesives with a film backing have been used to grasp convex objects [1], [3]. In [1], the gripper consists of two films which are oppositely aligned so that each is loaded in its preferred direction by pulling on a central bar (Fig. 1). Details of the design and manufacturing process are provided in [19].

For the active sensing application, we manufactured the PDMS film to be somewhat thicker than in the usual case, with a base layer of 510 μm (Table I). Doing so reduces the frequency of the M1 mode and reduces attenuation. However, making the base layer too thick reduces adhesive efficiency because the wedges no longer bend as in Fig. 1, left.

B. Piezoelectric Actuator and Sensor

For transducers we chose a polyvinylidene difluoride (PVDF) material for its flexibility and impedance match to the film. PVDF is a polymeric piezoelectric material (E = 2-4 GPa) which maintains the flexibility of the gripper after bonding. Moreover, its acoustic impedance is close to that of polyimide, which allows efficient wave transmission.

The dimensions of PVDF actuators and sensors were chosen to provide sufficient wave propagation in the high attenuation PDMS layer. As shown in Fig. 5, the width of the PVDF actuator affects the overall attenuation due to the tuning effect. For strong wave propagation, the width can be tuned to set the minimum attenuation close to the minimum of the substrate attenuation. When the tuned attenuation is small enough, a wider transducer usually transmits stronger waves because the wave displacement becomes greater. However, a larger area of PVDF film increases its capacitance, lowering the bandwidth of the sensing circuit, as discussed in the following section. Thus, we chose the dimensions of PVDF transducers as 13 x 30 mm for low attenuation in the M1 mode (Fig. 5) and a moderate capacitance of 1.37 nF.

Two actuator-sensor pairs are bonded to the proximal and distal regions of the adhesive film, respectively (Fig. 1). The actuators and receivers are aligned to have their polarization perpendicular to the preferred load axis. The Lamb wave propagates in this polarization direction (Fig. 2), minimizing the interference between adjacent regions. The actuators and sensors are cut from PVDF sheet (Measurement Specialties,

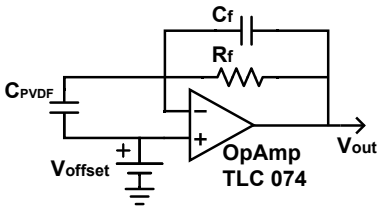

Fig. 6: Trans-impedance circuit for sensing the Lamb wave with PVDF ($C_f = 5\,\text{pF}$, $R_f = 1\,\text{M}\Omega$ $V_{offset} = 1.65\,\text{V}$).

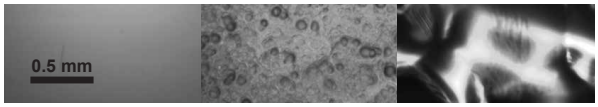

(a) Smooth (b) Fine (c) Wavy

Fig. 7: Microscope images of acrylic plates for pull tests.

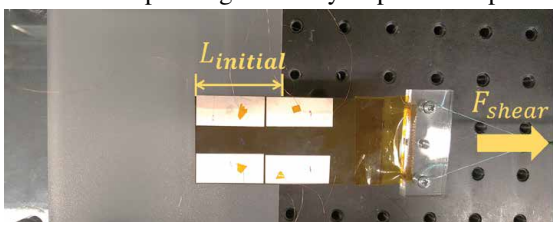

Fig. 8: Flat plate pull test; $L_{initial}$ varied from 2-5 cm.

metalized piezofilm sheets, 28 um thickness with silver ink) using a scalpel and bonded to the polyimide using a thin coating of spray adhesive (3M, Super 77). We leave a non-sensorized dead zone at the proximal end because our gripper does not make contact there, as seen in Fig. 1, right.

C. Sensor Circuit Design

To measure the Lamb wave a trans-impedance circuit was designed as in [20] (Fig. 6). The PVDF can be considered a current source with capacitance that varies the current in proportion to the strain. For a large current to voltage gain and a strong wave transmission, we need high R_f and a large PVDF area (thus high C_{PVDF}), which lowers the circuit bandwidth. The sensing circuit bandwidth is [21]:

$$BW = 1.4 \sqrt{\frac{GBW}{2\pi R_f (C_{PVDF} + C_f)}} \tag{2}$$

where GBW is the Op-amp gain bandwidth, and R_f, C_{PVDF} and C_f are as in Fig. 6. Thus, to maintain a sufficient BW with high R_f and C_{PVDF}, we chose an Op-amp with wide GBW (TI, TLC074, 10MHz GBW); the BW of Fig. 6 is 47kHz which covers the frequency response of the M1 mode.

IV. Experiments

A. Sensor validation using FTIR image and half-contact pull

We validated the theory of wave attenuation by using FTIR to confirm changes in contact area and adhesion. The adhesive film was placed on a glass panel with blue LED strips at its edge. Emitted light, corresponding to contact regions, was captured by a camera as the applied shear load varied. The free end of the adhesive film was clamped between two acrylic blocks to provide a relatively uniform tensile strain and shear load while pulling with a force scale (Mark10, Series4). Uniform contact and partial contact conditions were tested. For partial contact, a small piece of tape was attached on the PDMS side to take up some of the local shear load. The pull force was applied in steps of 2-5 N to a maximum of 24 N. The intensity of the emitted light was measured by the blue values of the digital image. The camera was set to have full-scale blue values corresponding to full wedge contact (with 100 kPa normal pressure). The wedge contact area was measured by summing the blue values of all pixels over each sensing area (Distal, Proximal).

Two different input signals were sourced to the actuator PVDFs from a function generator (Agilent, 33120A). First, an impulse signal (square wave burst mode, 50 μS pulse width, 20V peak to peak) was sourced to evaluate the frequency response of the Lamb wave to confirm theoretical predictions regarding frequency shifting and attenuation. Second, a Hanning windowed sine wave with 3.5 cycles was sourced to actuate a M1 Lamb wave mode with maximum wave energy. The response of the M1 mode confirms resonance rejection and allows a transient analysis with less computational effort. For both input signal cases, we tested 8 different initial contacts including uniform and partial contacts.

We measured each sensor by alternating the input signal. The input AC signal was switched using a SPDT switch (Analog Devices, ADG5436). For the impulse input signal, the measuring interval was 10 ms and for the 3.5 cycle sine wave, it was 3.3 ms. The sensor output of Fig. 6 was measured by an ADC sampling at 500 kHz.

In addition, we tested for interference between adjacent sensors using a half-contact pull test. On acrylic plate, the outputs of the two cases (entire area of the distal or proximal sensors) were measured with the Hanning windowed sine input. The pull force was measured by the force scale.

B. Pull test on flat plates with textures

We investigated if the sensor detects a precursor of impending slip failure and provides an estimate of the maximum load with different initial contact areas on various textured surfaces. We used three different acrylic plates (10 x 10 cm): clean smooth acrylic, finely textured or "frosted" acrylic, and wavy acrylic (Fig. 7). Each plate was clamped to a manual linear stage (Parker, 4411) to vary the initial contact area ($L_{initial}$ = 2-5 cm). The adhesive film was placed on the plate and pulled using a muscle lever (Cambridge Tech., Model 6900, Fig. 8). The initial tension was 3-5 N and the pull force ramped up to the level of slip failure. The ramping duration was 20 s and the force was measured at sampling rate of 200 Hz.

The input signal was a Hanning-windowed 3.5 cycle sine wave (center freq. 30 kHz). A micro controller (TI, TM4C123G) measured the sensor output and computed the peak-peak voltage, Vpp. This Vpp was used to estimate the attenuation of the Lamb wave. The same SPDT switch was used to alternate actuations with intervals of 3.3 ms. To enhance the signal to noise ratio, the non-contact outputs of both sensors were amplified to 2.9 Vpp.

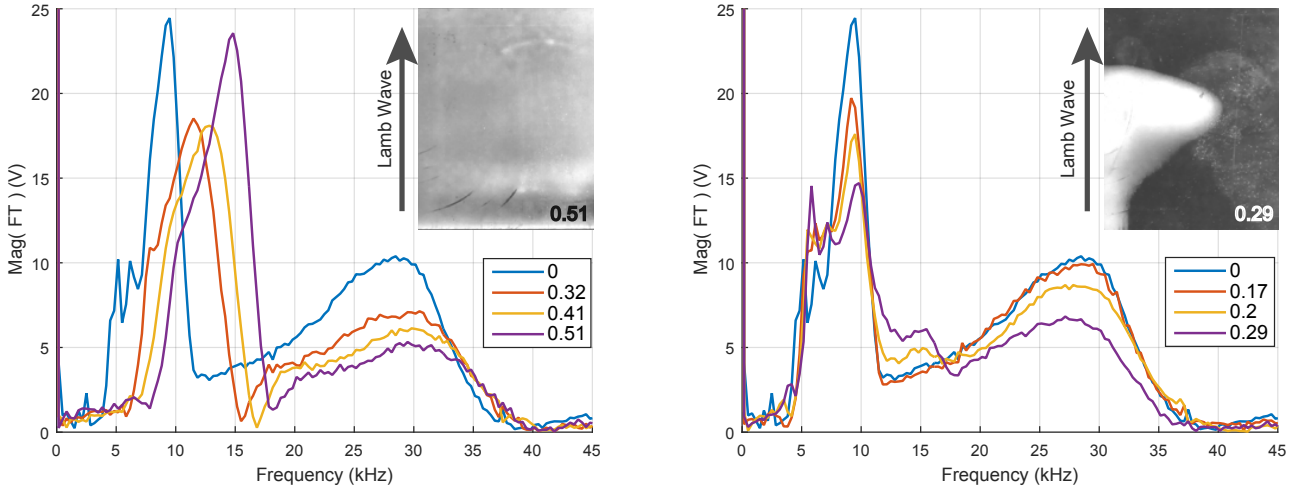

(a) (b)

Fig. 9: Magnitude of Fourier Transform (FT) of the proximal sensor output from the impulse input signal for (a) uniform contact, (b) partial contact. Legends indicate normalized contact areas measured by FTIR. Insets show corresponding post-processed FTIR images.

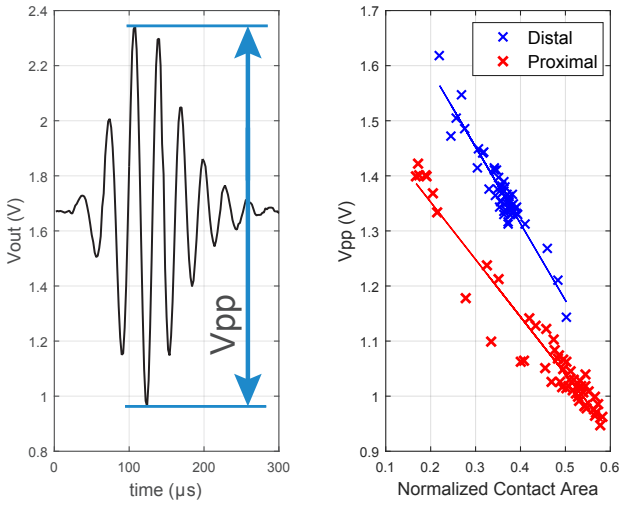

(a) (b)

Fig. 10: (a) Output of Hanning-windowed 3.5 cycle sine input. (b) Linear relationship between Vpp and normalized contact in two areas measured from FTIR test. Solid line is a linear fit with R^2 of 0.9 (Distal) and 0.94 (Proximal).

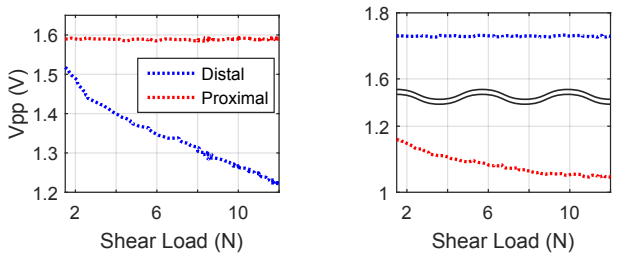

(a) (b)

Fig. 11: Sensor outputs show separation for (a) only distal area contact (b) only proximal area contact.

C. Lifting test on cylindrical object

We tested the sensor in a typical application of lifting a cylinder. For this test two patches of gecko inspired adhesives were cut to 39 x 85 mm, joined with polyimide tape in opposite orientations and connected to a central plate as shown in Fig. 1 to apply lifting loads. The target object was a hollow acrylic cylinder (10 cm diameter, 36 cm length, 640 g) with a 0.5 kg mass attached to the middle.

We investigated if the sensor can predict two common failure modes: proximal peeling and moment peeling. Proximal peeling occurs when the initial proximal contact is not sufficient to support the lifting force. The grasp fails when the remaining contact area at the distal end slips. Moment peeling occurs when the gripper makes contact far from the center of mass (COM). As the object is lifted, the COM exerts a substantial moment, peeling the contact at one side.

For the proximal peeling failure, we positioned the gripper with different initial contacts, above the center of the cylinder, aligning the loading axis with the COM. For the moment peeling failure, we placed the gripper far from the COM with sufficient initial contact to avoid proximal peeling.

We collected sensor outputs for over 30 trials for each test. The sensor output was obtained as in Section IV-B. The force was measured using the same force scale at 100 Hz.

V. Results

A. Sensor validation using FTIR image and half-contact pull

To validate the theory in Section II, the sensor output of an impulse input signal was analyzed using the Fourier Transform (FT) (Fig. 9). For both uniform and partial contacts, we found two main peaks at approximately 10 kHz and 30 kHz. As expected from Section II, the higher frequency peak was weaker due to higher attenuation and the lower frequency response showed sharp resonant responses around the major peak, while the higher frequency did not. The peak frequencies were slightly higher than predicted (6.3 kHz and 22.5 kHz),

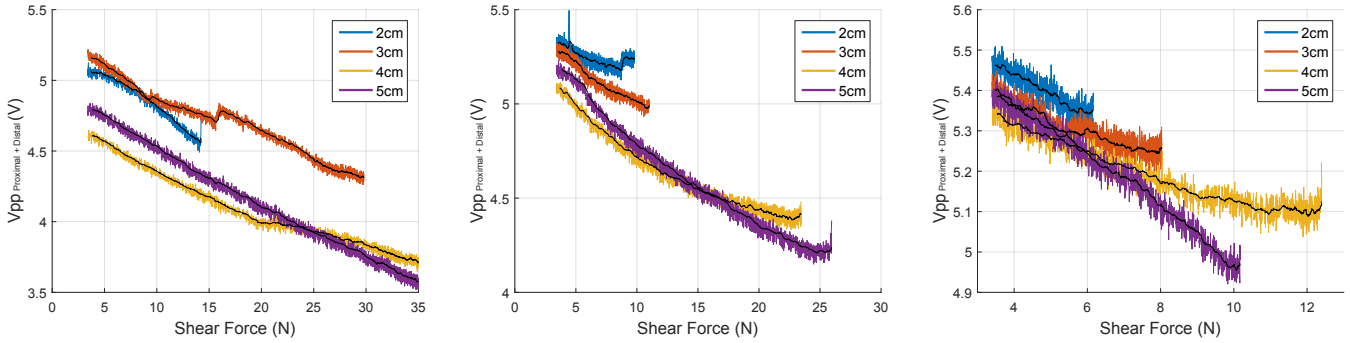

(a) (b) (c)

Fig. 12: Change in amplified sum of both sensor outputs ($\text{Vpp}_{\text{Proximal + Distal}}$) with increasing shear forces on (a) smooth, (b) fine textured, (c) wavy acrylic plates. Legends indicate varying $L_{initial}$, as in Fig. 8.

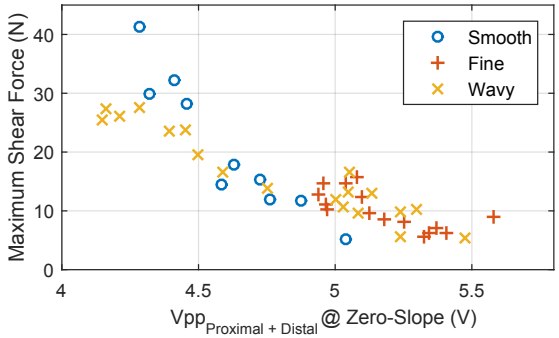

Fig. 13: Maximum shear load and sum of sensor outputs at the zero-slope phase before slip. Data include all $L_{initial}$.

TABLE II: Impending Failure detection on flat plates

	Failure detection rate	Impending Alert before slip (ms)	Input Force Rate (N/s)
Large Contact (4cm, 5cm)			
Fine Textured	100% (9 / 9)	136.3 (STD: 124.4)	1.4 (STD: 0.5)
Wavy Textured	100% (9 / 9)	166.6 (STD: 138.1)	0.8 (STD: 0.2)
Small Contact (2cm, 3cm)			
Smooth	80% (8 / 10)	65.9 (STD: 78.5)	1.3 (STD: 0.6)
Fine Textured	90% (9 / 10)	239.3 (STD: 249.0)	0.8 (STD: 0.3)
Wavy Textured	80% (8 / 10)	271.9 (STD: 232.9)	0.4 (STD: 0.1)

likely due to some uncertainty in assumed material properties or thickness variations.

The lower frequency response (≈10 kHz) shows distinct variations between uniform and partial contacts. In the uniform contact case (Fig. 9 (a)), the maximum peak shifts to a higher frequency as the contact increases. The shift is expected from dispersion theory with free boundary conditions versus fixed boundary conditions. The measured frequency shift was somewhat lower than predicted because it is difficult to achieve perfect engagement over the entire area. In the partial contact case (Fig. 9 (b)), however, the main peak frequency did not move as compared to the uniform contact case; the variation was only about 0.7 kHz. Moreover, the amplitude of the peak gradually decreased, while there was a slight increase in the frequency of the shifted signal (≈15 kHz). Because the lower frequency peak behaves differently between uniform and partial contacts, it is not a desired frequency for the sensor.

Unlike the previous results, the higher frequency response (≈30 kHz) shows a monotonic decrease as the contact changes, regardless of uniform or partial contact. Moreover, we found that the maximum frequency did not vary as much as the lower frequency response. In Fig. 9 (b), the dead-band of our sensor corresponds to normalized area of 0.17 which is equivalent to barely making contact. This finding allows us to actuate the system at the maximum frequency (30 kHz) and monitor the transient amplitude, which requires less computational effort than the FT. Therefore we use a Hanning windowed 3.5 cycle sine wave. The Vpp of the each sensor output signal (Fig. 10a) was plotted along with the measured contact area (Fig. 10b). The figure shows a linear relationship between Vpp and actual contact areas in each sensing region, with $R^2 > 0.9$.

The result of the half-contact pull shows that the two sensing units do not interfere. For both contact cases, only the contacting sensor output changes while the other remains virtually unchanged (Fig. 11). We achieve this isolation by minimizing wave leakage from weak cross wave propagation and alternation of each sampling. From this interference test, we conclude that the sensor output in Fig. 10b is an independent measure of real contact area on each sensing region or cell. Thus, if an array of sensors are implemented, they can measure the contact of a large area.

The response of the distal area is higher than the proximal area. We think this is caused by small uncertainties of the circuit components, and area differences in the PVDF strips. In the following experiments, we amplified the two sensor outputs to be equal at 2.9 V.

B. Pull test results on textured plates

To test the sensor response under actual loading scenarios, we placed the adhesive on three different acrylic plates and applied a shear force with four different initial contact areas. We measured 9-10 trials for each surface-initial area pair, and computed the sum of the two sensor outputs (Vpp) (Fig. 12). In general, the Vpp attenuates increasingly as the shear force increases and the contact area increases in proportion. In the following, we propose a method to estimate the maximum shear load and predict impending failure.

To estimate the maximum supportable shear load, we used the sensor output where Vpp does not change, namely the zero-slope phase. When the gecko wedges are under a large shear load, increasing the load no longer produces additional bending of the wedges but instead begins to stretch them. This stretching does not increase the contact area or the

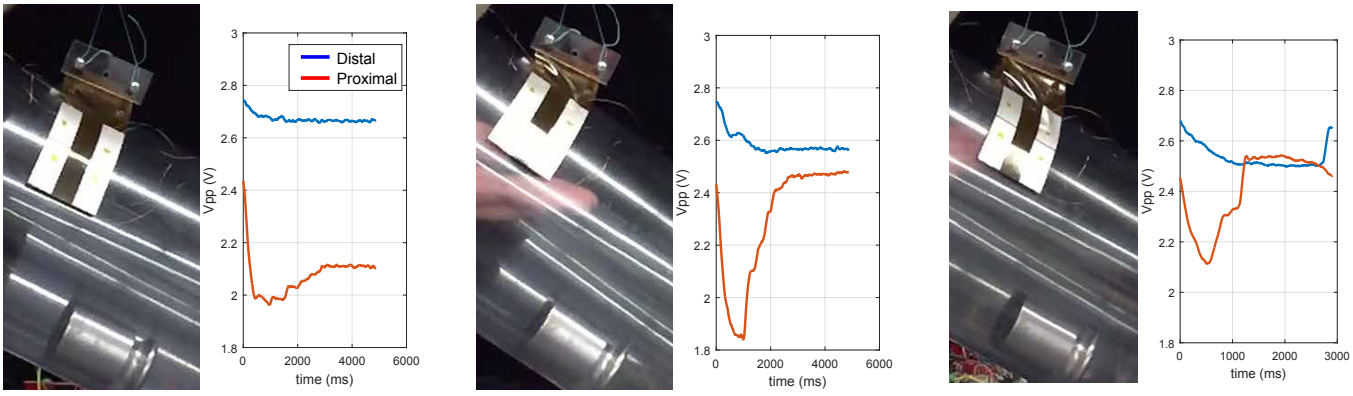

Fig. 14: Lifting a cylindrical object with misaligned center of mass: frames of high speed video and sensor output history for (a) stable grasping success, (b) unstable grasping success, (c) grasping failure (moment peeling)

TABLE III: Impending Failure detection on a cylindrical Object

	Slip Failure detection rate	Impending Alert before slip (ms)	Input Force Rate (N/s)	False Negative Warning
Proximal Peeling	85.0% (17 / 20)	143.7 (STD : 141.7)	3.5 (STD : 1.6)	42.8% (9 / 21)
Moment Peeling	87.5% (14 / 16)	164.5 (STD : 135.2)	3.0 (STD : 1.5)	31.6% (6 / 19)

supportable shear load [9]. The effects of wedge stretching and contact area saturation are seen in Fig. 12. As the shear load increases, the slope of the sensor output decreases to zero indicating the upper limit of contact area. The Vpp at zero-slope phase is plotted with the maximum shear load in Fig. 13. Regardless of the initial overlap, $L_{initial}$, the maximum shear load correlates to the point at which the real contact area (which depends on surface smoothness) is no longer growing. To obtain this figure, we filtered the data of slipped failure cases (moving average filter, window length = 15 samples). The zero-slope was scanned from a least square fit of 50 adjacent points. The maximum shear load increased linearly as more attenuation occurred in Vpp at zero-slope. Although the variation in maximum shear load at the same Vpp is not negligible ($\approx$10 N), the zero-slope Vpp provides an estimate of whether the desired shear force can be achieved from a given contact condition. The uncertainty of this estimate can be compensated by using the impending failure prediction in the following discussion.

An impending slip failure can be detected by slope reversal of the sensor outputs. Slope reversal is where the sensor output starts to increase even with increasing shear load. When more shear force is applied after the zero-slope phase, some wedges start to lose contact while others maintain adhesion. This local detachment decreases the overall contact area until the adhesion cannot meet the shear load [9]. This decrease of contact area can be detected by the slope reversal of the sensor output.

We detect slope reversal as follows. First, the slopes of the sensor output are measured by the same least square fit as for zero-phase detection. The m^{th} sampled data point is considered to be a slope reversal when it meets the following criteria:

$$[\ S(m) > S_{std}\ ] \vee [\ A(m) - A_F(m) > 3A_{std}\ ] \\ \vee [\ A(m) - \overline{A(m-7)} > 2A_{std}\ ] \quad (3)$$

where $S(m)$ is the least squares regression slope of 50 samples prior to the m^{th} sample, S_{std} is the standard deviation of slopes, A is the sum of two sensor outputs, A_F is the filtered A, and $\overline{A(m-7)}$ is the mean of 5 adjacent data around the $(m-7)^{th}$ (50 ms prior to m) sample. The first block of eq. 3 tests positive slope, and the other two compensate for delays from the filter and the linear fit. We applied eq. 3 to 9-10 trials of slipped cases for each texture-initial contact combination to predict the slope reversal within 1 s before failure.

Table II shows the detection success rate using eq. 3 and the detection time before failure. For the large initial contact area, we predicted all failures approximately 150 ms before they occurred. Note that on smooth acrylic no failure occurs because the adhesion limit exceeds the muscle lever's force range. On small initial contact areas, the success rate was $>$80% and the average detection time was 1.7 times earlier than for large contact. This detection time increase means that the sensor provides preliminary alerts rather than indications of imminent failure. It arises because with a small contact area, local detachments cause rapid drops of adhesion, which are difficult to capture with the current sampling rate. With the current rate, eq. 3 triggers for two samples or longer in 93% of detection cases; presumably, acceptable force rates could be up to two times greater than in Table II. From Fig. 10a, the maximum Vpp sampling rate can be 10 times faster. Under a linearity assumption, 20 times greater force rates than in Table II could be measurable. For fast response, however, the Signal to Noise Ratio (SNR) should be improved so that fewer samples are required for eq. 3.

In a real application, the slope reversal can be used as a warning signal for poor adhesion. However, it is not a decisive metric that presages slip failure. Even after the slope reversal, the gecko wedges can locally readjust their contact, recovering adhesion. Thus, we suggest a failure prediction strategy that combines the zero-slope sensor level and slope reversal in the following section.

C. Results of lifting test on a cylindrical object

We tested the sensor in a practical application of lifting a cylindrical object with known weight. For both COM aligned and misaligned pulling we found that the slope reversal usually indicates impending failure. However, if the gripper maintained sufficient contact area, even with a slope reversal, the gripper did not slip (Fig. 14). More importantly, the level of proximal contact area is a critical factor in grasping even with similar overall contact area.

From these findings, we impose an additional criterion using the levels of sensor outputs. The criterion includes the slope reversal (eq. 3), zero-slope, and sufficient overall and proximal contact areas as follows:

$$[\text{ eq. (3)} \vee [\ |S(m)| < S_{std}\ ]\ ] \wedge [\ A(m) > P\ ]\ \wedge [\ A_{prox}(m) > P_{prox}\ ] \quad (4)$$

where A_{prox} is the proximal sensor output, P is the threshold for sufficient overall area, and P_{prox} is the threshold for sufficient proximal area. The P was set as 4.8 V where maximum shear force is more than the object weight in Fig. 13; P_{prox} was conservatively set as 2.1 V.

The detection results (Table III) show that the sensor can predict slip failure approximately 150 ms in advance with $>80\%$ accuracy. Note that we implemented sensors on only one side of gripper; if slip occurs on the opposite side, the sensor can hardly detect the rapid contact changes with the current sampling rate. If both sides have sensors, we believe the detection rate will be higher. The alert time ranges from 8-511 ms, meaning that the sensor can signal a controller at least 8 ms prior to the slip. This is advantageous over dynamic sensing approaches that accompany the onset of sliding [20]. The rate of false negative warnings was relatively high because we intentionally performed unstable grasping. In real applications, the gripper is expected to have mostly reliable grasping. Thus, a controller can be designed to reengage the object when the sensor produces an alert, despite some false negatives.

VI. Conclusion and Future Work

An active sensing method measures the contact area of adhesive films by monitoring the attenuation of guided Lamb waves. The sensor uses PVDF strips bonded to the backing layer. The attenuation of the Lamb waves changes according to contact boundary conditions, which depend on how effectively the adhesive engages a surface. Using FTIR optical imaging, we showed that Lamb wave attenuation is proportional to the real contact area. In addition, by monitoring changes (zero-slope and slope reverse) from the sensor, adhesion failure was signaled approximately 150 ms before a slip, with a detection rate of $>80\%$.

In future work, sensor arrays will be implemented on all adhesive regions of a gripper and a flexible PCB will be employed to reduce noise for fast response. The sensors can then be used in closed loop control for grasp monitoring. Studies of grasping soft materials and application to soft grippers are another promising extension. For finer spatial resolution in an array of cells one could also employ a tomography method.

References

[1] E. W. Hawkes, H. Jiang, D. L. Christensen, A. K. Han, and M. R. Cutkosky, "Grasping without squeezing: Design and modeling of shear-activated grippers," *IEEE Trans. Robotics*, 2017.

[2] E. W. Hawkes, H. Jiang, and M. R. Cutkosky, "Three-dimensional dynamic surface grasping with dry adhesion," *Int. J. Robotics Research*, vol. 35, no. 8, pp. 943–958, 2016.

[3] H. Jiang, E. W. Hawkes, C. Fuller, M. A. Estrada, S. A. Suresh, N. Abcouwer, A. K. Han, S. Wang, C. J. Ploch, A. Parness *et al.*, "A robotic device using gecko-inspired adhesives can grasp and manipulate large objects in microgravity," *Sci. Robot.*, vol. 2, p. eaan4545, 2017.

[4] S. Kim, M. Spenko, S. Trujillo, B. Heyneman, D. Santos, and M. R. Cutkosky, "Smooth vertical surface climbing with directional adhesion," *IEEE Trans. robotics*, vol. 24, no. 1, pp. 65–74, 2008.

[5] M. P. Murphy, B. Aksak, and M. Sitti, "Gecko-inspired directional and controllable adhesion," *Small*, vol. 5, no. 2, pp. 170–175, 2009.

[6] L. F. Boesel, C. Greiner, E. Arzt, and A. Del Campo, "Gecko-inspired surfaces: a path to strong and reversible dry adhesives," *Advanced Materials*, vol. 22, no. 19, pp. 2125–2137, 2010.

[7] S. Song, D.-M. Drotlef, C. Majidi, and M. Sitti, "Controllable load sharing for soft adhesive interfaces on three-dimensional surfaces," *PNAS*, p. 201620344, 2017.

[8] J.-P. Roberge, W. Ruotolo, V. Duchaine, and M. Cutkosky, "Improving industrial grippers with adhesion-controlled friction," *IEEE RA-Letters*, vol. 3, no. 2, pp. 1041–1048, 2018.

[9] X. A. Wu, D. L. Christensen, S. A. Suresh, H. Jiang, W. R. Roderick, and M. Cutkosky, "Incipient slip detection and recovery for controllable gecko-inspired adhesion," *IEEE RA-Letters*, vol. 2, no. 2, pp. 460–467, 2017.

[10] E. V. Eason, E. W. Hawkes, M. Windheim, D. L. Christensen, T. Libby, and M. R. Cutkosky, "Stress distribution and contact area measurements of a gecko toe using a high-resolution tactile sensor," *Bioinspiration & biomimetics*, vol. 10, no. 1, p. 016013, 2015.

[11] N. Wettels and A. Parness, "Advances in fibrillar on-off polymer adhesive: Sensing and engagement speed," in *2014 IEEE/RSJ IROS*, 2014, pp. 4266–4271.

[12] J.-B. Ihn and F.-K. Chang, "Pitch-catch active sensing methods in structural health monitoring for aircraft structures," *Structural Health Monitoring*, vol. 7, no. 1, pp. 5–19, 2008.

[13] V. Giurgiutiu, *Structural health monitoring: with piezoelectric wafer active sensors*. Academic Press, 2007.

[14] B. W. Drinkwater, M. Castaings, and B. Hosten, "The measurement of a 0 and s 0 lamb wave attenuation to determine the normal and shear stiffnesses of a compressively loaded interface," *J. the Acoustical Society of America*, vol. 113, no. 6, pp. 3161–3170, 2003.

[15] J. L. Rose, *Ultrasonic guided waves in solid media*. Cambridge University Press, 2014.

[16] F. Simonetti, "Lamb wave propagation in elastic plates coated with viscoelastic materials," *J. the Acoustical Society of America*, vol. 115, no. 5, pp. 2041–2053, 2004.

[17] B. Pavlakovic, M. Lowe, D. Alleyne, and P. Cawley, "Disperse: a general purpose program for creating dispersion curves," in *Rev. progress in quantitative nondestructive evaluation*. Springer, 1997, pp. 185–192.

[18] S. Santhanam and R. Demirli, "Reflection of lamb waves obliquely incident on the free edge of a plate," *Ultrasonics*, vol. 53, no. 1, pp. 271–282, 2013.

[19] P. Day, E. V. Eason, N. Esparza, D. Christensen, and M. Cutkosky, "Microwedge machining for the manufacture of directional dry adhesives," *J. Micro and Nano-Manufacturing*, vol. 1, no. 1, 2013.

[20] M. R. Cutkosky and J. Ulmen, "Dynamic tactile sensing," in *The Human Hand as an Inspiration for Robot Hand Development*. Springer, 2014, pp. 389–403.

[21] J. Graeme, *Photodiode amplifiers: op amp solutions*. McGraw-Hill, Inc., 1995.